https://doi.org/10.21012/FC10.238496

FRACTURE PROPERTIES OF ALKALI ACTIVATED MORTARS

GIULIA BAIETTI [*], LORENZA CARABBA [**], GIOVANNI QUARTARONE [‡], CHRISTIAN CARLONI [†], STEFANIA MANZI [§] AND MARIA CHIARA BIGNOZZI [§§]

[*] University of Bologna (UNIBO)
Viale Risorgimento 2, Bologna, Italy
e-mail: giulia.baietti2@unibo.it, www.dicam.unibo.it

[**] University of Bologna (UNIBO)
Via Terracini 28, Bologna, Italy
e-mail: lorenza.carabba3@unibo.it, www.dicam.unibo.it

[‡] University of Bologna (UNIBO)
Via Terracini 28, Bologna, Italy
e-mail: giovanni.quartarone2@unibo.it, www.dicam.unibo.it

[†] Case Western Reserve University
10900 Euclid Ave, Cleveland, Ohio, USA
e-mail: christian.carloni@case.edu, www.engineering.case.edu

[§] University of Bologna (UNIBO)
Via Terracini 28, Bologna, Italy
e-mail: stefania.manzi4@unibo.it, www.dicam.unibo.it

[§§] University of Bologna (UNIBO)
Via Terracini 28, Bologna, Italy
e-mail: maria.bignozzi@unibo.it, www.dicam.unibo.it

Key words: Alkali activated mortar, three-point bend test, fracture energy, DIC, fracture process zone

Abstract: In this paper, three different coal fly ash-based alkali activated mortars are studied. The three different mortars are obtained using the same binding system but different types (i.e. silica sand or expanded perlite) and sizes of aggregates. Small-scale beams are constructed together with additional specimens for material characterization. The small-scale beams are notched and loaded in a three-point bend setup to investigate the fracture properties of the three mixtures. The setup utilized follows the draft of the ACI 446 report on the fracture testing of concrete. The fracture energy is determined from the work of fracture and results highly dependent on the type of aggregate rather than its dimension. Digital image correlation is employed to obtain the displacement and therefore strain components on the side surface of the specimens in order to investigate the crack propagation and determine the size of the fracture process zone, which appears to be similar to the one of a cement-based mortar.

1 INTRODUCTION

In an attempt to reduce the CO_2 emissions related to the production of cement, a new class of cement-free materials known as alkali activated materials (AAMs) has rapidly grown in interest in the last two decades. AAMs have been increasingly investigated as an emerging technology and as a suitable alternative to ordinary Portland cement (OPC)-based mortars and concrete [1-5]. AAMs are based on the reaction between a solid aluminosilicate source and an alkali activator to obtain a mainly amorphous 3D network of aluminosilicates with binding properties. One of the main advantages of AAMs is the possibility of using waste powders as amorphous aluminosilicate source, which react in sodium and/or potassium hydroxide and silicate solutions [6]. This aspect makes AAMs particularly interesting to obtain sustainable materials and to pursue a circular economy approach. Although the properties of AAMs resemble the properties of cement-based mortars and concrete, a change in the solid aluminosilicate source and activator provide a wide spectrum of material properties that require a full characterization still not fully explored in the literature [7-12]. As a consequence of the variability of the chemical and physical properties of the AAMs, the mechanical properties are expected to vary and in particular the fracture properties, which have not been studied in depth for this class of materials [13- 16]. The focus of this paper is the investigation of the fracture properties of three different AAMs, which are obtained by using the same binding system but different types (i.e. silica sand or expanded perlite) and sizes of aggregates. Three-point bend (TPB) tests are carried out on notched beams. Two sizes of the beams are considered for each mortar type. Digital image correlation (DIC) is used to plot the strain and crack opening profiles along the ligament for different points of the load response. An attempt to measure quantitatively the size of the fracture process zone (FPZ) through DIC analysis is proposed. It is observed that for one of the three AAMs, the FPZ is relatively small and therefore can fully develop for the larger of the two sizes of the notched beams. The fracture energy is computed employing the work of fracture method and an argument is made by the authors about the reliability of such type of measurement.

2 MATERIALS AND METHODS

2.1 Materials

Coal fly ash (FA), sourced from the Italian coal-fired power station of Torrevaldaliga Nord (Rome), was used as precursor for the synthesis. FA was characterized by a low content of calcium and iron oxides, while nearly 80 wt% was constituted of silicon and aluminum oxides [12]. 8 M sodium hydroxide (NaOH, supplied by Sigma-Aldrich) and sodium silicate (SiO_2/Na_2O ratio = 2.07, ρ_{bulk} = 1.53 g/cm^3 kindly supplied by Ingessil Srl, Verona, Italy) solutions were used as alkaline activators. The SiO_2/Al_2O_3 and Na_2O/SiO_2 molar ratios were kept constant for all mixtures and equal to 3.52 and 0.12, respectively, while the amount and the type of the aggregate were changed. The three mortars featured three different types and sizes of aggregates. The mortar herein named FS was obtained by employing fine silica sand with a fixed grain size distribution according to EN 196-1 standard [17]. The maximum aggregate size d_{max} was equal to 2 mm and the density of the aggregate was ρ = 2.64 g/cm^3. The mortar herein named CS had coarse silica sand with d_{max} = 6.0 mm and ρ = 2.68 g/cm^3. Finally, the mortar labelled as EP featured expanded perlite with d_{max} = 2.8 mm and ρ = 0.95 g/cm^3. The three mortars were poured into prismatic molds of different sizes (for both material characterization and TPB specimens) in two layers. Each layer was vibrated on a shaker for 60 s. All molds were sealed in plastic bags and cured at T = 21 ± 2°C for 24 h. Specimens were de-molded after 24 h and cured sealed in plastic bags (i.e. sealed conditions) in the same laboratory conditions until were used to determine the mechanical and physical properties of the mortars.

2.2 Physical and mechanical characterization

The physical and mechanical properties of mortars were determined at 28 and 300 days, which corresponds to the age of testing. The bulk density (ρ_{bulk}) and water absorption were measured on prisms of dimensions 40 mm ×

40 mm × 20 mm. The bulk density was calculated as the dry mass divided by the geometrical volume, while the water absorption was calculated as the difference between the wet and the dry mass divided by the dry mass.

Prisms of dimensions 40 mm × 40 mm × 160 mm were used to determine the mechanical properties of the mortars. The elastic modulus was calculated according to EN 13412 [18]. Flexural (R_f) and compressive (f_c) strength were determined according to EN 196-1 [17] by means of a 100 kN Amsler Wolpert testing machine. All results are presented as average of at least two measurements.

2.3 Methods

Two different sizes of the notched beams were tested. The nominal dimensions were either 70 mm (width B) × 70 mm (depth D) × 300 mm (length L) or 35 mm (width B) × 35 mm (depth D) × 200 mm (length L). The notch was cut after the specimens were stored in laboratory condition for at least 100 days. A special blade was used to obtain a sharp tip in order to force the crack propagation along the axis of the notch and limit the variability of the results, which appears to be hardly achieved with a non-sharp tip [13-16]. The notch length a_0 was equal to D/3 and its width was 3 mm. The net span S was equal to 3D. Table 1 summarizes the list of specimens with their labels, which report the size of the specimen and the type of mortar. It should be pointed out that for the sake of brevity only the actual measurement of the length of the notch is reported in Table 1. It was measured at the end of the test at three locations across the width. The average measurement of the crack length for each specimen with the coefficient of variation (CoV) are reported in Table 1. The actual measurements of the width and depth were taken at 6 different locations, while 8 measurements of the length of the specimens were taken. The average and CoV of these measurements are not reported herein but were used in the calculations presented in the next Sections. The same TPB set-up, described in [19] and used for concrete specimens to study the effect of the width on the fracture response, was used in this campaign. A sketch of the set-up and a photo of a specimen are provided in Figure 1a and b.

Table 1: Name of specimens, measurement of the notch with CoV, peak load with its average with CoV

Specimen	a_0 (CoV) [mm]	P_{max} [kN]	$\bar{P}_{max}$ (CoV) [kN]
70×70×300_FS _1	24.69 (0.030)	2.59	
70×70×300_FS _2	23.19 (0.028)	2.62	2.60 (0.005)
70×70×300_FS _3	22.61 (0.019)	2.60	
70×70×300_FS _4	21.63 (0.019)	2.61	
70×70×300_CS_1	21.13 (0.054)	2.25	
70×70×300_CS_2	25.07 (0.044)	2.20	2.27 (0.032)
70×70×300_CS_3	24.39 (0.047)	2.26	
70×70×300_CS_4	25.44 (0.012)	2.37	
70×70×300_EP_ 1	23.38 (0.005)	0.59	
70×70×300_EP_ 2	23.39 (0.030)	0.74	0.68 (0.129)
70×70×300_EP_ 3	23.31 (0.014)	0.77	
70×70×300_EP_ 4	22.92 (0.018)	0.62	
35×35×200_FS _1	11.31 (0.010)	0.82	
35×35×200_FS _2	11.33 (0.016)	0.69	0.76 (0.086)
35×35×200_FS _3	11.46 (0.024)	0.77	
35×35×200_ CS_1	12.29 (0.041)	0.68	
35×35×200_ CS_2	12.08 (0.041)	0.62	0.65 (0.047)
35×35×200_ CS_3	11.66 (0.034)	0.64	
35×35×200_ EP_ 1	11.88 (0.023)	0.20	
35×35×200_ EP_ 2	10.55 (0.015)	0.18	0.20 (0.100)
35×35×200_ EP_ 3	11.94 (0.010)	0.22	

Two linear variable displacement transformers (LVDT) were mounted on a horizontal steel plate and reacted off a Z-shaped top plate that was placed between the top loading block and the specimen. The average of the two LVDT readings is the load point displacement δ. A clip-on gauge was used to measure the crack mouth opening displacement (CMOD) and control the test. The test rate (CMOD control) was chosen to reach the peak load between 150 and 210 seconds from the beginning of the test.

a

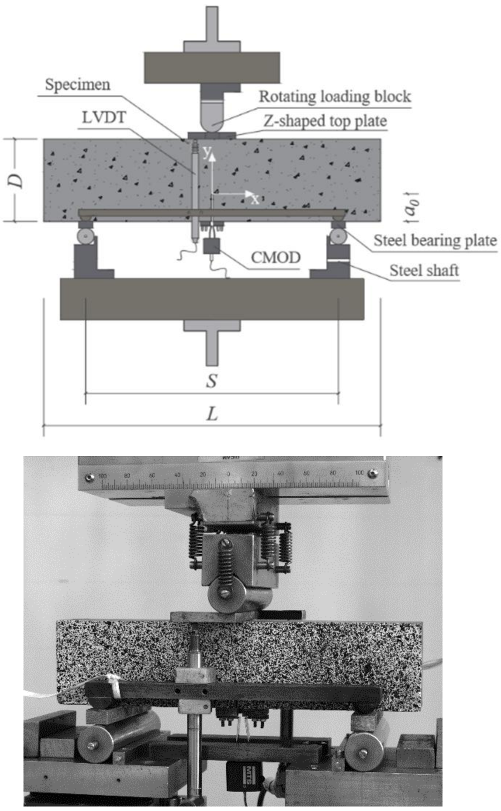

b

Figure 1: a) Sketch of the test set-up; and b) photo of a representative specimen

The initial test rate v_1 was equal to 0.0001 mm/s. When the load reached 80% of the peak load in the descending branch of the response, the test rate v_2 was increased to 0.0003 mm/s. Finally, when the load reached 35% of the peak load in the descending branch, the test rate v_3 was increased to 0.0005 mm/s until the end of the test. For two specimens for each type of mortar and size of the beam, DIC was employed to evaluate the displacement field and derive the strain field on one of the side surfaces of the specimen.

3 EXPERIMENTAL RESULTS

3.1 Physical and mechanical properties of mortars

The physical and mechanical characterization of the three mortars was performed at 28 and 300 days as described above, and the results are reported in Table 2, Table 3, Table 4.

Table 2: Physical properties at 28 and 300 days

	Bulk density [g/cm^3] (CoV)		Water absorption [%] (CoV)	
	28 days	300 days	28 days	300 days
FS	2.02 (0.005)	2.11 (0.005)	6.55 (0.020)	5.89 (0.010)
CS	2.00 (0.005)	2.11 (0.005)	8.05 (0.006)	7.55 (0.011)
EP	1.11 (0.036)	1.26 (0.008)	30.47 (0.011)	25.84 (0.001)

Table 3: Mechanical properties at 28 days

	R_f [MPa] (CoV)	f_c [MPa] (CoV)	E_{28} [GPa] (CoV)
FS	10.0 (0.020)	65.3 (0.018)	19.7 (0.041)
CS	9.4 (0.085)	47.6 (0.059)	17.8 (0.056)
EP	3.6 (0.028)	14.7 (0.034)	1.2 (0.083)

Table 4: Mechanical properties at 300 days

	R_f [MPa] (CoV)	f_c [MPa] (CoV)	E_{300} [GPa] (CoV)
FS	12.3 (0.008)	71.7 (0.036)	22.9 (0.014)
CS	12.1 (0.041)	63.7 (0.011)	20.5 (0.025)
EP	4.2 (0.071)	16.6 (0.024)	4.7 (0.094)

3.2 Load responses

Table 1 provides the peak load $P_{\max}$ of each specimen, the average $\bar{P}_{\max}$ for each family with the coefficient of variation. The load responses in terms of applied load P versus δ and applied load P versus CMOD are reported in Figure 2a and b, respectively, for specimen 70×70×300_FS _2. The P-δ curve, referred to the readings of the two LVDTs, is compared with the P-δ curve of the same specimen obtained from DIC in Figure 2a. In order to compute the displacement δ from DIC, the displacement on the surface of the specimen near the load point was computed by averaging the DIC displacements over an 8 mm × 8 mm square area. This square area is marked in blue in Figure 2a. The average displacement was also computed for two square areas of the same size as the first and located at the centroid of the cross-sections corresponding to the supports. Finally, δ was calculated as the difference of the average displacement of the top square area and the average of the two displacements obtained from the squares placed at the supports. The P-δ curve from DIC described above is plotted with blue diamond markers in Figure 2a. As damage near the load point might occur, a second square was placed closer to the actual load point to verify the trend of the P-δ curve. The second square is marked in red in Figure 2a and the corresponding curve is plotted with a red dashed line. It can be observed that the DIC curves are basically coincident, which suggests that damage near the load point might be negligible. As the DIC curves are compared with the P-δ curve obtained from LVDT readings, it can be noted that the initial stiffness is different. This was observed also in [19] and it might be due to small adjustments that LVDTs undergo during the first phase of the test. A similar trend was observed for the small specimens. The load responses for specimen 35×35×200_ CS_2 are reported in Figure 3. It should be noted that for all 35×35×200 specimens, only one LVDT was used in order to have a full field DIC image of the specimen. This expedient was adopted in order to compute an additional value of δ from DIC, which corresponds to placing the support squares near the supports themselves rather than at their centroid. These squares are marked in green in Figure 3a. The corresponding P-δ curve, which uses the top blue square and the green squares at the supports, is plotted with a dashed green line. It can be concluded that damage at either support is limited and does not affect the measurements of δ. The initial linear portion of the P-δ or P-CMOD curve can be used to determine the elastic modulus. For the sake of brevity, only the results corresponding to the P-CMOD curve are reported in this paper. The CMOD can be computed as [20]:

$$\text{CMOD} = \frac{a6PS}{EBD^2} V_1(\alpha) \tag{1}$$

$$V_1(\alpha) = 0.76 - 2.28\alpha + 3.78\alpha^2 - 2.04^3 + \frac{0.6}{(1-\alpha^2)} \tag{2}$$

$\alpha = a_0/D$. The slope of the P-CMOD curves was computed between 20% and 50% of the peak load $P_{\max}$ and used to back-calculate the elastic modulus. The average value of the elastic modulus $\bar{E}_{\text{CMOD}}$ is reported in Table 5.

Table 5: Elastic modulus from P-CMOD response

Specimen	$\bar{E}_{\text{CMOD}}$ [MPa]
70×70×300_CS_1 70×70×300_CS_2 70×70×300_CS_3 70×70×300_CS_4	15563
70×70×300_EP_1 70×70×300_EP_2 70×70×300_EP_3 70×70×300_EP_4	3613
70×70×300_FS_1 70×70×300_FS_2 70×70×300_FS_3 70×70×300_FS_4	18419
35×35×200_CS_1 35×35×200_CS_2 35×35×200_CS_3	13069
35×35×200_EP_1 35×35×200_EP_2 35×35×200_EP_3	2458
35×35×200_FS_1 35×35×200_FS_2 35×35×200_FS_3	14893

The values of the elastic modulus obtained from Eqs. (1) and (2) are consistent with the results reported in Table 5. Similar values could be obtained if the load point formula is used although results would depend on whether the slope of the *P*-δ curve is obtained from the LVDT or DIC readings.

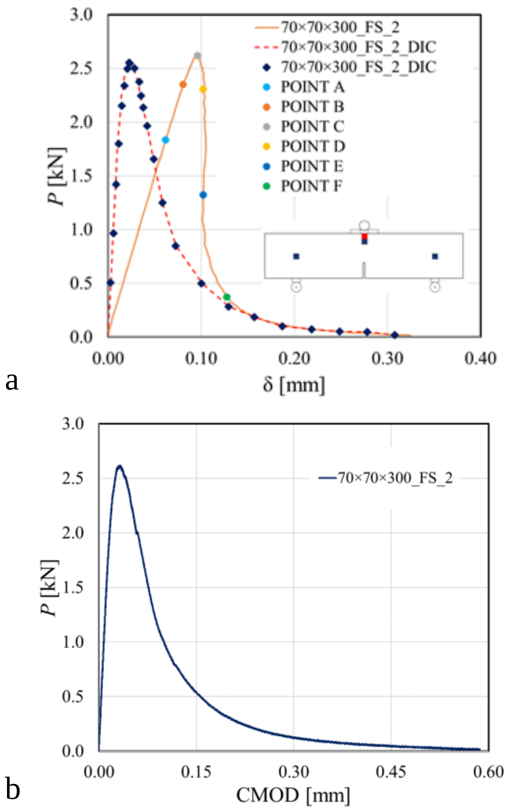

Figure 2: Representative 70×70×300 specimen: a) comparison of the *P*-δ curves obtained from LVDT and DIC measurements; b) *P*-CMOD curve

3.3 Failure modes

All specimens failed due to the propagation of a crack from the tip of the notch. The crack pattern was essentially straight. Small kinks occurred as the crack propagated but overall the crack pattern was within the width of the initial notch as it can be observed from Figure 4a and b that show cross-section and side of the beam.

4 DISCUSSION

4.1 Fracture energy

The fracture energy G_F was computed using the concept of work of fracture. The self-weight was also taken into account. A description of the full procedure can be found in [19]. If *W* is the work of the applied load, then (without considering the effect of the self-weight)

$$G_F = \frac{W}{B(D - a_0)} \tag{3}$$

W is computed as the area under the *P*-δ curve.

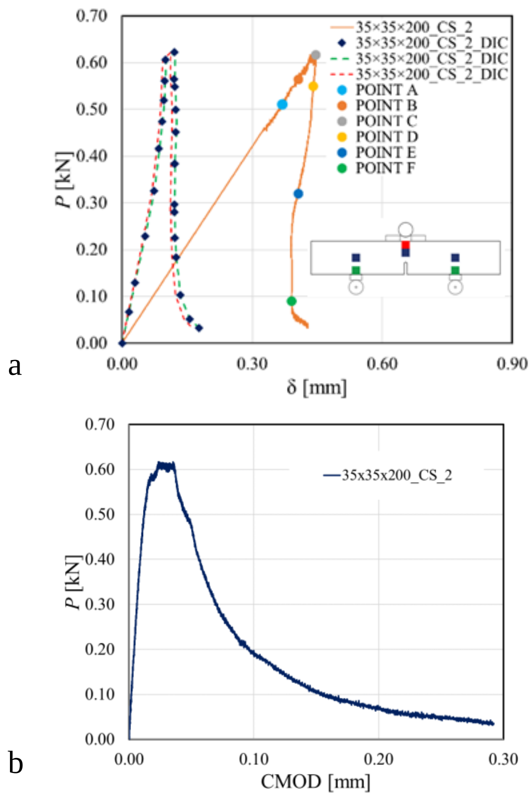

Figure 3: Representative 35×35×200 specimen: a) comparison of the *P*-δ curves obtained from LVDT and DIC measurements; b) *P*-CMOD curve

Figure 4: Failure mode of 70×70×300_FS _2 specimen: a) cross-section; and b) side view

Only the P-δ curves obtained from DIC were used to compute W. In fact, as the small specimens were equipped only with one LVDT, there was no control on a possible rotation of the specimen out-of-plane, which would translate in different readings of the two LVDTs. Table 6 provides the average fracture energy $\bar{G}_F^{DIC}$ for each family of specimens and its coefficient of variation. The values of the fracture energy from corresponding 70×70×300 and 35×35×200 specimens are consistent although slightly higher for smaller specimens, which in part might be due to the size effect [21, 22] that reflects in a higher peak load for smaller specimens. G_F does not vary significantly as the size of the maximum diameter of the silica sand changes from 2 mm to 6 mm. A substantial difference in the fracture energy can be observed if FS and CS specimens are compared with EP specimens.

Table 6: Fracture energy and CoV

Specimen	$\bar{G}_F^{DIC}$ [N/m] (CoV)
70×70×300_CS_1 70×70×300_CS_2 70×70×300_CS_3 70×70×300_CS_4	56.4 (0.204)
70×70×300_EP_1 70×70×300_EP_2 70×70×300_EP_3 70×70×300_EP_4	11.4 (0.272)
70×70×300_FS_1 70×70×300_FS_2 70×70×300_FS_3 70×70×300_FS_4	52.1 (0.079)
35×35×200_CS_1 35×35×200_CS_2 35×35×200_CS_3	61.5 (0.296)
35×35×200_EP_1 35×35×200_EP_2 35×35×200_EP_3	14.1 (0.503)
35×35×200_FS_1 35×35×200_FS_2 35×35×200_FS_3	61.7 (0.206)

4.2 Strain profile and crack opening

The strain field obtained from DIC was used to plot the horizontal strain component ε_{xx} along the ligament for different points of the load response, in attempt to study the fracture process zone (FPZ), which is one of the features of quasibrittle materials [21]. The coordinate system x,y used in this Section is shown in Figure 1a. In order to plot the strain profiles, ε_{xx} was averaged across a 10 mm strip centered with respect to the notch for any value of y.

The strain profiles for specimen 70×70×300_FS_2 are shown in Figure 5a. The value of the strain $\varepsilon_{t,sp}^{E_{300}}$ corresponding to the splitting tensile strength (f_t') was computed using the relationship (reported in [23]) between f_t' and R_f provided in Table 4 and using the elastic modulus E_{300} at 300 days reported in Table 3 as well. A vertical dashed line marks the value of $\varepsilon_{t,sp}^{E_{300}}$ in Figure 5a, which is equal to 0.00030 for FS specimens. The points selected for the strain profiles are marked in Figure 2a. The intersection of the strain profile with the dashed line marks the beginning of the FPZ, i.e. the region of softening behavior that develops from the tip of the notch [21]. At point C (peak load), the extension of the FPZ, i.e. the distance from the tip of the notch to the intersection between the strain profile and the dashed line, is approximately 2.5 mm. At points D and E the extension of the FPZ is approximately 15 mm and 30 mm, respectively. It should be noted that the FPZ forms before the peak load and at 50% of the peak load (point E) in the descending branch of the response the FPZ is still expanding. The FPZ at point E has covered the majority of the ligament, which indicates that for the rest of the test the propagation of the crack will not have the characteristics of a self-similar propagating crack because of the presence of the compressive zone on top of the beam. This observation makes the authors question if Eq. 3 can be used to obtain the true value of the fracture energy as the formula assumed that the cracks extends under similar conditions until failure.

In order to investigate further the size of the FPZ, the crack opening was studied by plotting the difference of the horizontal displacement Δu across the ligament. Δu was computed by averaging the horizontal component of the displacement in two 5 mm (width) × 2.5 mm (height) rectangles symmetrically placed at a distance of 10 mm (same as the width of the strip used to obtain the strain profiles) with respect to the ligament. Δu is the difference between the averages of the displacements of the two rectangles. Δu is plotted in Figure 5b for the same specimen 70×70×300_FS_2.

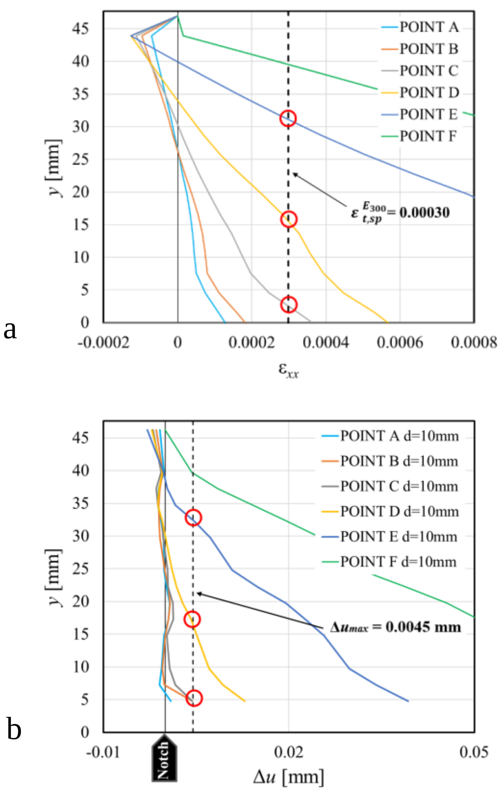

Figure 5: Strain (a) and Δu (b) profiles along the ligament for specimen 70×70×300_FS_2 for different points of the load response

The maximum elastic elongation corresponding to the strain $\varepsilon^{E300}_{t,sp}$ was computed as:

$$\Delta u_{\max} = \varepsilon^{E300}_{t,sp}\xi \tag{4}$$

ξ is the distance between the centroids of the two rectangles used to determine the average of the displacements. ξ =15 mm in this study. Δu_{max} for FS specimens is equal to 0.005 mm, while for CS and EP specimens Δu_{max} equals to 0.005 mm and 0.007 mm, respectively. Δu_{max} for 70×70×300_FS specimens is marked with a vertical dashed line in Figure 5b. It can be noted that the distance of the intersection of the Δu curve and the dashed line from the tip of the notch corresponds to the extension of the FPZ obtained from the strain profiles.

The crack opening w_f corresponding to the end of the FPZ can be estimated as [24]:

$$w_f = \frac{5.6G_F}{f'_t} \tag{5}$$

The values of the crack opening w_f for the 70×70×300_FS family is equal to 0.043 mm. This value was obtained by employing the average fracture energy reported in Table 6 for the larger FS specimens and the splitting tensile strength obtained from the flexural strength [23]. It should be noted that the value of Δu corresponding to the physical separation of the two surfaces of the crack can be computed as:

$$\Delta u_f = w_f + \Delta u_{\max} \tag{6}$$

For specimens belonging to the 70×70×300_FS family, $\Delta u_f = 0.048$ mm. Thus, from Figure 5b it can be inferred that the FPZ is fully established between points E and F, which means that the size of the FPZ is approximately between 16$d_{\max}$ and 20$d_{\max}$. The plots of the strain profile and crack opening were repeated for the 70×70×300_CS and 70×70×300_EP family. In addition, the values of w_f for these two families were equal to 0.047 mm and 0.027 mm, respectively. Thus, for the same families, Δu_f equals to 0.052 mm and 0.034 mm, respectively. It could be concluded that, by looking at the corresponding ε_{xx} and Δu profiles (not reported for the sake of brevity), the size of the FPZ was in between 5$d_{\max}$ and 6d_{max} for the 70×70×300_CS specimens and between 9d_{max} and 10$d_{\max}$ for the 70×70×300_EP specimens. It is interesting to note that the size of the FPZ is not uniquely related to the size of the aggregate even for the FS and CS mortars that employ the same type of aggregate.

The same plots were repeated for the

35×35×200 families of specimens. As an example, the strain and Δu profiles were plotted in Figure 6 for specimen 35×35×200_CS_2. The value of w_f for the 35×35×200_CS family was equal to 0.051 mm and $\Delta u_f = 0.056$ mm, which means that the FPZ was not fully established at point E.

The values of w_f for the 35×35×200_FS and 35×35×200_EP families were equal to 0.051 mm and 0.034 mm, respectively, which provide $\Delta u_f = 0.056$ mm and $\Delta u_f = 0.041$ mm. The plots of ε_{xx} and Δu for these two families of specimens confirm that for the smaller specimens the FPZ was not fully developed.

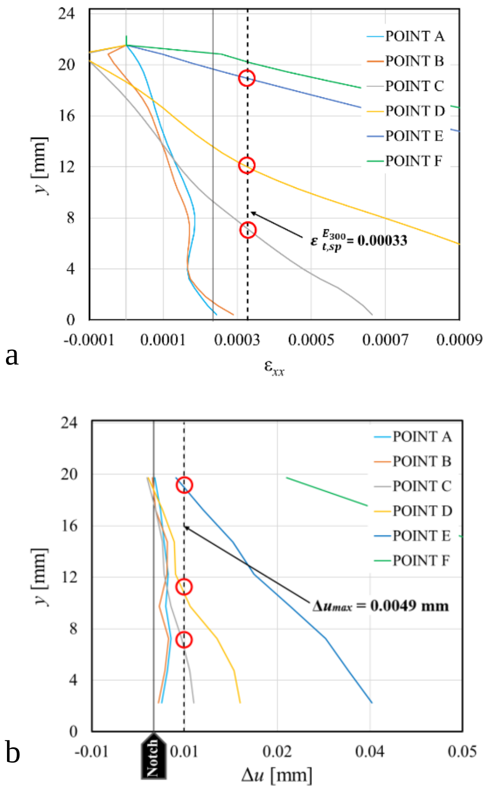

Figure 6: Strain (a) and Δu (b) profiles along the crack ligament for specimen 35×35×200_CS_2 for different points of the load response

5 STRAIN CONTOUR PLOT

Contour plots of the horizontal strain component ε_{xx} for 4 points (B, C, D, and E) of the load response of Figure 3a are shown in Figure 7. The points selected correspond to 90% of P_{max} in the ascending branch of the curve, P_{max}, and 90% and 50% of P_{max} in the descending branch. The color scale was chosen so that the maximum tensile strain was approximately equal to $\varepsilon^{E300}_{t,sp}$ in order to be consistent with the dashed line reported in Figure 6. This expedient allowed to identify the region in red as the region where the strain was higher than $\varepsilon^{E300}_{t,sp}$ and therefore corresponded to the FPZ. It is interesting to note that the FPZ expands in the post peak region both in length and width. It appears to be almost of the same width between points D and E. At point E, as observed earlier, the FPZ extends for almost the entire height of the specimen and therefore since at this point the value of Δu_f is still not reached the FPZ does not have room to fully develop.

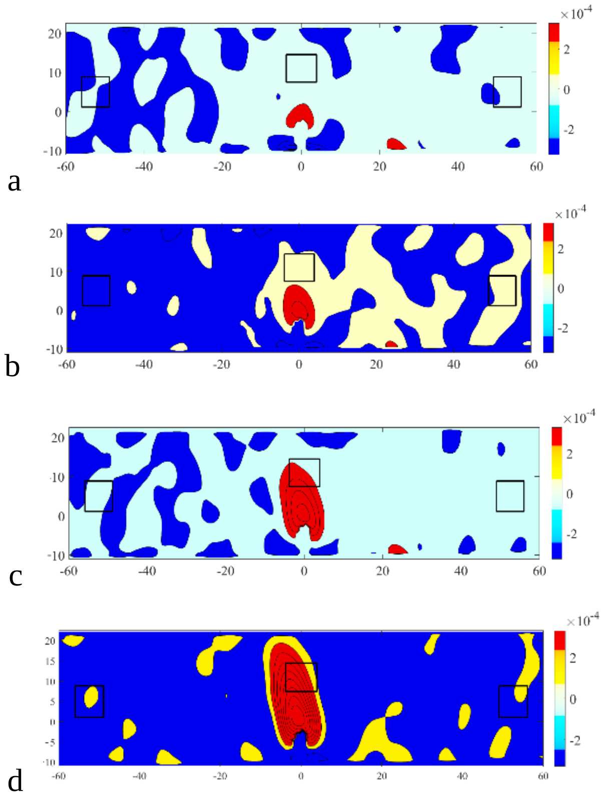

Figure 7: Contour plots of strain component ε_{xx} for points B (a), C (b), D (c) and E (d) of the load response shown in Figure 3a

6 SIZE EFFECT

The average peak load $\bar{P}_{\max}$ of each family of specimens can be used, in terms of nominal stress σ_N, to build the double log plot typically used to study the size effect [21, 22, 24, 25].

The plot is shown in Figure 8. It is interesting to note how the slope of the line connecting the points corresponding to two sizes of the same AAM is very similar.

This is expected for specimens FS and CS because they have a similar size of the FPZ and even the larger size of the specimens for these two mortars can barely accommodate the fully developed FPZ. On the other hand, the FPZ of EP specimens is estimated to be relatively smaller than the height of the larger specimens. Nevertheless, the slope of the lines connecting the points relative to EP specimens is similar to the other AAMs. A possible justification can be found in the results of Table 1.

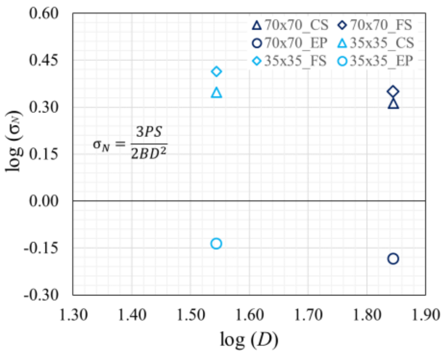

Figure 8: Logarithmic plot of σ_N versus D for the three AAMs

The CoV of $\bar{P}_{\max}$ for both sizes of the EP specimens is relatively high compared to the others. Thus, the plot of σ_N should be critically considered for these specimens. It should pointed out that after the failure of the specimens, the fracture surfaces of the EP specimens revealed that the distribution of the perlite was not uniform across the width, which could be potentially a cause of the large variability of the results of the EP specimens.

7 CONCLUSIONS

This study presented an experimental work to study the fracture properties of three alkali activated mortars (AAMs) that were obtained by using the same binding system but different types (i.e. silica sand or expanded perlite) and sizes of aggregates. Three-point bend tests of notched beams of two different sizes were performed for all three AAMs. Digital image correlation (DIC) was used to obtain the displacement and strain profiles along the ligament and the load-deflection curves. DIC was successfully employed to measure the extension of the fracture process zone (FPZ) and gain an insight into the fracture properties. The experimental results suggest that the size of the FPZ and the fracture energy depend on the type of aggregate used in the mixture rather than its size. Thus, the size of the FPZ is related to the size of the aggregate but the relationship is not unique for the three AAMs herein studied. The full development of the FPZ occurs in the descending branch of the load response and as it covers the majority of the ligament, the remainder of the load response is associated with a non-self-similar crack propagation, which in turn made the authors questioned whether the work of fracture method is appropriate to determine the fracture energy. Finally, it was observed that for the AAM that employed expanded perlite, the results were quite scattered and therefore the size effect plot might not be reliable.

REFERENCES

[1] J. Provis, "Alkali-activated materials," *Cem Concr Res*, 2017.

[2] Carabba L., M. Santandrea , C. Carloni , S. Manzi and M. Bignozzi , "Steel fiber reinforced geopolymer matrix (S-FRGM) composites applied to reinforced concrete structures for strengthening applications: A preliminary study.," *Composites Part B: Engineering*, vol. 128, p. 83–90., 2017.

[3] Singh B., G. Ishwarya , M. Gupta and S. Bhattacharyya, "Geopolymer concrete: A review of some recent developments," *Constr Build Mater* , vol. 85, p. 78–90., 2015.

[4] Monticelli C., M. Natali , A. Balbo, C. Chiavari , F. Zanotto and S. Manzi, "Corrosion behavior of steel in alkali-activated fly ash mortars in the light of their microstructural, mechanical and chemical characterization.," *Cem Concr Res* , vol. 80, p. 60–8., 2016.

[5] Bernal S.A. and J. Provis , "Durability of Alkali-Activated Materials: Progress and Perspectives," *J Am Ceram Soc* , vol. 97, p. 997–1008., 2014.

[6] Scrivener KL., V. John and E. Gartner , *Eco-efficient cements: Potential, economically viable solutions for a low-CO2, cement-based materials industry,* Paris, 2016.

[7] Duxson P, J. Provis , G. Lukey and J. van Deventer, "The role of inorganic polymer technology in the development of “green concrete.”," *Cem Concr Res,* vol. 37, pp. 1590-7, 2007.

[8] G. G. J. C. B. H. K. H. Sturm P., "Sulfuric acid resistance of one-part alkali-activated mortars," *Cem Concr Res,* vol. 109, p. 54–63., 2018.

[9] D. Davidovits J. and J. Therm Anal , "Geopolymers inorganic polymeric new material," vol. 37, p. 1633–56., 1991.

[10] K. Barbosa V.F.F. MacKenzie, "Thermal behaviour of inorganic geopolymers and composites derived from sodium polysialate.," *Mater Res Bull,* vol. 38, p. 319–31., 2003.

[11] Zhao R and J. Sanjayan , "Geopolymer and Portland cement concretes in simulated fire," *Mag Concr Res,* vol. 63, p. 163–73, 2011.

[12] Rickard W.D.A, G. Gluth and K. Pistol, "In-situ thermo-mechanical testing of fly ash geopolymer concretes made with quartz and expanded clay aggregates.," *Cem Concr Res,* vol. 80, p. 33–43., 2016.

[13] Z. Pan, J. G. Sanjayan and B. V. Rangan, "Fracture properties of geopolymer paste and concrete," *Magazine of Concrete Research,* vol. 63, no. 10, p. 763–771, 2011.

[14] Pradip N. and K. Prabir , "Fracture properties of GGBFS-blended fly ash geopolymer concrete cured in ambient temperature," *Materials and Structures* , p. 50:32, 2017.

[15] P. Sarker, R. Haque and K. Ramgo, "Fracture behaviour of heat cured fly ash based geopolymer concrete," *Materials and Design* , vol. 44 , p. 580–586, 2013.

[16] Z. Xie, Zhou H.F., L. Lu and Z. Chen, "An investigation into fracture behavior of geopolymer concrete with," *Construction and Building Materials,* vol. 155, p. 371–380, 2017.

[17] *EN 196-1:2005 Methods of testing cement – part 1: Determination of strength..*

[18] *UNI EN 13412:2003: Determination of the Elastic Modulus in Compression.*

[19] Carloni C., M. Santandrea, and G. Baietti , "Influence of the width of the specimen on the fracture response of concrete notched beams," *Engineering Fracture Mechanics,* Accepted manuscript.

[20] H. Tada, P. Paris, and G. Irwin , "The stress analyisis of cracks handbook," *Del Research Corporation,* 1976.

[21] Z. Bažant, Fracture in concrete and reinforced concrete, Northwestern University, Evanston: Bažant Z.P., 1983, pp. 281-316.

[22] Z. Bažant, "Size Effect in Blunt Fracture: Concrete, Rock, Metal," *Journal of Engineering Mechanics,* vol. 110, no. 4, 1984.

[23] *Eurocode 2 - Design of concrete structures. Part 1-1: General rules and rules for building ENV 1992-1-1.*

[24] Z. P. Bažant and J. Planas, Fracture and size effect in concrete and other quasibrittle materials, CRC press, 1997.

[25] Z. Bažant, "Instability, ductility, and size effect in strain-softening concrete," *ASCE J Eng Mech Div,* vol. 102, no. 2, pp. 331-334, 1976.

[26] Z. P. Bažant, "Size effect in tensile and compression fracture of concrete structures: computational modeling and design," *Fracture Mechanics of Concrete Structures,* vol. 3, pp. 1905-22, 1998.